EUROPEAN ORGANIZATION FOR NUCLEAR RESEARCH

CERN-EP/90-03
January 10,1990

LIQUID-XENON CALORIMETER FOR THE DETECTION OF ELECTROMAGNETIC SHOWERS

A. Baranov*), V. Baskakov*), G. Bondarenko*), I. Gavrilenko**), B. Dolgoshein*), O. Kozodaeva**), S. Konovalov**), V.N. Lebedenko*), S. Muraviev**), A. Shmeleva**), V. Tcherniatin*) and P. Vassiliev**)

ABSTRACT

The energy and spatial resolution of the 40 l liquid-xenon calorimeter was measured. For electrons in the energy region 1–6 GeV, the resolutions are: $\sigma_E/E = 3.4/\sqrt{E}(\%)$; $\sigma_x = 4.6/\sqrt{E}$ (mm). The details of construction and running of such a device are discussed.

(Submitted to Nucl. Instrum. Methods)

*) Moscow Physical Engineering Institute, Moscow, USSR

**) Lebedev Physical Institute, Moscow, USSR

1. DESCRIPTION OF THE CALORIMETER

Since 1974 [1] several large liquid-argon calorimeters (LAr) have been built and used in high-energy physics experiments [2–6]. These calorimeters have a sampling structure using iron or uranium plates. The best energy resolution was obtained with aluminium electrodes [7, 8], but at the cost of the apparatus having to be as large as ~ 3 m longitudinally. In order to reduce the size of the calorimeter, it is interesting to use liquid xenon. The relevant properties of LAr and LXe are listed in table 1 [9]. The attractive characteristics of LXe are its small radiation length, small W-value and Fano factor. It is possible to build LXe calorimeters of good energy resolution and of smaller dimensions than with LAr.

Here we present the 40 l LXe calorimeter performance, and the results of its test measurements done at the Serpukhov accelerator. The calorimeter was designed for recording electrons and photons in the energy range of 1 to 10 GeV.

Figures 1a,b show the design of the LXe calorimeter. The multilayer ionization chamber (7) was placed in a cryostat (1, 2). The inner, stainless-steel cylindrical vessel (1), of 50 cm in diameter and 60 cm long, was filled with liquid xenon. A vacuum of 5×10^{-4} Torr between the two cylinders and the 10 layers of aluminized Mylar foils served as thermal insulation.

In order to save a lot of xenon and to obtain a more homogeneous temperature, the aluminium segments (4, 10) were placed on both sides and at the bottom of the electrode system (7). The bottom segment (4) was joined to the copper bar (5) that is immersed in a reservoir containing liquid nitrogen LN_2 (6). This bar serves as a heat exchanger and it was supplied with a heating and temperature-control system.

The liquid xenon was kept cold by a LN_2-fed refrigeration loop placed above the electrode system. About 40 l of liquid xenon are needed to submerge the detector. The cryostat volume was not completely filled: there was a 10 cm buffer of gaseous xenon in contact with the liquid above the electrode system. At 1 atm of saturated vapour pressure, xenon exists in the liquid phase in a temperature range of 4 degrees (T_{boil} = 165 K).

Two different electrode configurations were used. The first one was for the *energy-resolution measurements;* both anode and cathode planes were made from 50 μm thick Al foils, with 12 mm gap between anode and cathode. All anodes were connected, and so were all cathodes. The diameter of the active zone of the electrodes was 25 cm, and its total length along the beam was 50 cm. The total LXe and Al thickness was 17.5 and 2.5×10^{-2} radiation lengths (X_0) respectively. Such a configuration was chosen to achieve the best ratio of active material (LXe) length to passive material (Al) length, and therefore to reduce the sampling fluctuations.

The second electrode configuration was for the *position-resolution measurements;* both anode and cathode planes were made from Cu-clad fibre-glass sheets. The gap width between anode and cathode was 6 mm. The 350 μm copper foil was glued to both sides of a 1 mm thick fibre-glass sheet. Strips (10 mm width, 1 mm separation) were machined from a copper foil. Successive anode and cathode strips were connected (fig. 2). The active area was thus subdivided into 24×1 cm^2 readout columns. The depth of the electrode system along the beam axis was 55 cm. The total LXe and electrodes thicknesses were $17.0X_0$ and $0.8X_0$, respectively.

The charge analysis system had 1 channel in the first configuration and 24 channels in the second one. Each channel was made up of a low-noise charge-sensitive preamplifier, a shaping amplifier ($\tau_{diff} = \tau_{int} = 3$ μs), and a LeCroy QADC. Figure 3 shows a block diagram of the electronics. The calibration of the amplifiers was done with a generator using a precise amplitude and a calibration capacitance. The measured value of the noise-equivalent charge of the amplifier was 5×10^4 electrons in the first configuration (whole detector capacitance C_{det} = 5 nF) and was 4×10^3 electrons per column (C_{det} = 300 pF) in the second configuration. The signal analysis system had a non-linearity of less than 0.2% over the whole energy range.

Figure 4 shows schematically the gas and cryogenic system. When the apparatus is not in operation, the Xe gas is stored in ballast bottles (5) of 40 l each at a pressure of 40 atm. Before filling the storage system, the bottles are kept under a vacuum of 10^{-3} Torr during 72 hours, at 100°C temperature. All tubes connecting the different elements of the gas system are made of stainless steel. The system designed to achieve this vacuum consists of a vacuum pump (10), zeolite traps (7), and an ion pump (8).

For good energy resolution, it is necessary to collect the total ionization charge produced by the electromagnetic showers. The purity of the liquid xenon is thus crucial to the operation of the calorimeter. The xenon was purified in the gaseous as well as in the liquid phases using a Ca reactor (3) and a discharge purifier (2) respectively. Porous titanium filters (4) protect the gaseous system against calcium oxide dust. The principle of action of the discharge purifier was elaborated by Obadovsky et al. [10]. In our case, the discharge purifier (2) is a stainless-steel 5 l vessel with a cooling and a thermostabilization systems. Inside there are two Ti electrodes placed 1 mm apart. A high voltage of 20–25 kV is applied to the electrodes. The electrical discharge causes Ti evaporation over the whole volume of liquid xenon. The absorption of impurities by dispersed Ti dust is very active. The impurity level of the liquid xenon after going through the purifier was examined by a special ionization test chamber (1). This chamber had two electrodes, 90 mm in diameter and 10 mm apart. The X-rays of $E_\gamma = 20$ keV were injected into the chamber through a 0.5 mm Al window. The time of injection was 0.5 μs. The shape of the current signal was analysed. Our system allows us to purify xenon down to a concentration of electronegative impurities corresponding to 5 cm free path for the electrons in the liquid xenon. The purification of $\sim$ 30 m^3 of xenon gas takes 6 to 7 days. A detailed description of our purification system is given in ref. [11].

The working volume of the calorimeter was maintained at a vacuum of 10^{-3} Torr at 100°C temperature during 72 hours before being filled with purified xenon. Nevertheless, after the calorimeter was filled, the mean free path of electrons was reduced (from 5 cm to 1 cm in the case of Al electrodes, and to 0.3 cm in the case of fibre-glass electrodes). Over one month, the xenon purity then remained stable. The reduction of purity at the time of filling may be caused by a strong release of gas from the electrodes surfaces and from other elements of the calorimeter at the temperature of 165 K.

2. TEST BEAM LAYOUT

The tests of the LXe calorimeter have been made using a secondary beam at the Serpukhov accelerator. The momentum of the particles could be varied in the range from 1 to 6 GeV/c. Figure 5 is a schematic view of the test layout. The incident beam was defined by the four-fold coincidence of the scintillation counters S_1–S_4. The electrons were selected by two threshold Cherenkov counters C_1, C_2, which gave a rejection coefficient of $\epsilon_e/\epsilon_h = 3.6 \times 10^6$ at an electron efficiency of $\eta_e = 90\%$. The beam momentum was measured by a magnetic spectrometer consisting of a magnet (M) and three multiwire proportional chambers (PC_1–PC_3) with cathode readout. The spatial accuracy in the proportional chambers was $\sigma_x = 37$ μm. The accuracy $\sigma(p)/p$ in the momentum measurement was calculated to be 0.4% at 1 GeV/c and 0.9% at 5 GeV/c. The magnetic spectrometer allows the point of entry of the particle into the calorimeter to be measured with an accuracy of $\sigma_e = 80$ μm.

3. EXPERIMENTAL RESULTS

Figure 6 shows the spectrum of 2.25 GeV/c secondary particles measured by the LXe calorimeter without magnet spectrometer analysis. Figures 7 and 8 show the spectra of 2.25 GeV/c and 4.75 GeV/c momentum electrons selected with the aid of Cherenkov counters. Figures 9 and 10 show the $E - pc$ distributions for electrons with $p = 2.25$ and 4.75 GeV/c; E is the electron energy

measured by the LXe calorimeter, p the momentum measured by the magnet spectrometer, and c is the velocity of light. The distribution was fitted with a Gaussian, giving an energy resolution at 4.75 GeV/c of $\sigma_E/E = (1.7 \pm 0.2)\%$. Figure 11 shows the dependence of the energy resolution on the electron energy. In the energy range of 1–6 GeV it can be written as:

$$\sigma_E/E = 3.4/\sqrt{E(\%)} \ ,$$

where E is in GeV.

The spatial resolution of the LXe calorimeter was obtained from the $X_F - X_S$ distribution (fig. 12), where X_S is the coordinate of particle entry into the calorimeter, measured by the magnetic spectrometer, and X_F is the coordinate of the axis of the electromagnetic shower in the LXe calorimeter; X_F has been measured using two methods:

1. Centre-of-gravity method:

$$X_F = \sum_{k=1}^{n} \frac{Q_k X_k}{Q_\Sigma} = \sum_{k=1}^{n} \frac{Q_k(k - 1/2)d}{Q_\Sigma} \ ; \qquad Q_\Sigma = \sum_{k=1}^{n} Q_k \ .$$

Here Q is the charge collected on the k^{th} strip, d is the strip's width, and n is the number of strips.

2. Minimum χ^2 method:

We assume that the transverse distribution of the charge in a shower can be given by the expression [13]:

$$\frac{dQ}{dx} \simeq \frac{\epsilon_0}{2b} \, e^{-\Delta/b} \ ,$$

where $\epsilon_0 = \int_{-\infty}^{+\infty} (dQ/dx) \cdot dx$, $\Delta = |X_k - X_F|$, is the parameter characteristic of the shower width, and X_k the coordinate of the centre of the k^{th} strip. The coordinate of the electromagnetic shower axis was determined by minimizing the expression:

$$\chi^2 = \sum_{k=1}^{n} \frac{(Q_{tk} - Q_{ek})^2}{\sigma_k^2} \ ,$$

with

$$Q_{tk} = \begin{cases} \epsilon_0[1 - \exp(-\ell/b)\cosh(\Delta/b)] & \text{for } \Delta < d/2 \ , \\ \epsilon_0 \exp(-\Delta/b)\sinh(\ell/b) & \text{for } \Delta \geq d/2 \ , \end{cases}$$

Q_{ek} = charge collected on the k^{th} strip,
σ_k = background of k^{th} electronic channel,
$\ell = d/2$,
n = number of strips.

Figure 13 shows the results of the measurement of the spatial resolution by the two methods at electron energies of 2.7, 4.2, and 5.7 GeV/c. The energy dependence of the spatial resolution can be written as:

$$\sigma_x = 4.6/\sqrt{E} \ (\text{mm}) \ ,$$

where E is in GeV. The difference between the experimental points and the calculated ones at E = 2.7 GeV/c can be explained by the rise of an electronics background in σ_x at this energy.

Figure 14 shows the value of the coordinate X_F versus the coordinate X_S as defined for fig. 12. The spatial resolution has been measured for 1 cm and 2 cm strips at E = 3.8 GeV/c. The results are:

$$\sigma_x\,(2\Delta = 2\,\text{cm}) = (2.3 \pm 0.5)\,\text{mm}$$

$$\sigma_x\,(2\Delta = 1\,\text{cm}) = (2.0 \pm 0.3)\,\text{mm}$$

There is no difference, within the errors.

The efficiency of electron–hadron separation was also investigated using the total energy deposition in the calorimeter and the transverse shower distribution. The χ^2 value was calculated for each event:

$$\chi^2 = \sum_{k=1}^{n} \frac{(Q_{tk} - Q_{ek})^2}{\sigma_k^2} \,.$$

Also for each event, the parameters b and ϵ_0 were determined by minimization of the χ^2.

Figure 15 shows the dependence of the rejection factor e/h (electrons against hadrons) on the electron efficiency ϵ_e in the case when only the total energy deposition in the LXe calorimeter is used. For example, for $\epsilon_e = 90\%$, $e/h = 1.2 \times 10^2$. The additional information from the transverse distribution of the shower (parameter b) improves the rejection by a factor of 1.5.

The liquid-xenon appproach seems better suited for collider experiments. The main advantage is its small size in comparison with the liquid-argon calorimeter. There seems to be no problem that could not be solved in constructing or running such a detector in a real experiment.

We wish to thank R. Schuvalov and R. Krasnokutsky for giving us the amplifiers and for useful discussions. We thank V. Kantzerov for his help in this work.

REFERENCES

[1] W. Willis and V. Radeka, Nucl. Instrum. Methods **120** (1974) 221.

[2] L. Ladage, The TASSO liquid argon calorimeters, Proc. Int. Conf. on Instrumentation for Colliding Beam Physics, Stanford, 1982 (SLAC-250, Stanford, 1982), p. 180.

[3] C. Fabjan et al., Nucl. Instrum. Methods **141** (1977) 61.

[4] J.M. Cobb et al., Nucl. Instrum. Methods **158** (1979) 93.

[5] J. Engler et al., Nucl. Instrum. Methods **120** (1974) 157.

[6] S. Aronson et al., Nucl. Instrum. Methods **A269** (1988) 492.

[7] C. Cerri et al., Nucl. Instrum. Methods **214** (1983) 217.

[8] T. Doke et al., Nucl. Instrum. Methods **237** (1985) 475.

[9] Th. Lindblad et al., Nucl. Instrum. Methods **215** (1983) 183.

[10] I. Obodovsky et al., Zh. Tekh. Fiz. **50** (1980) 2028.

[11] I. Gavrilenko et al., preprint FIAN N252, Moscow (1984).

[12] A. Baranov et al., Instrum. & Exp. Tech. **28** (3, Part 1) (1985) 543 [transl. from Prib. & Tekh. Eksp. **3** (1985) 40].

[13] Yu.B. Bushnin et al., Nucl. Instrum. Methods **106** (1973) 493.

Table 1

Physical properties of liquid argon and liquid xenon [9]

Properties	LAr	LXe
Atomic number Z	18	54
Atomic mass A	40	131
Triple point (K)	85	163
Density at triple point (g/cm^3)	1.41	2.96
Gas-to-liquid ratio	784	518
Radiation length (cm)	13.9	2.87
Molière radius (cm)	10	5.73
W-value (eV/ion pair)	23.3	15.6
Fano factor	0.107	0.041
Mobility ($m^2/V \cdot s$)	0.048	0.22

Figure captions

Fig. 1a,b Sketch of the calorimeter cryostat: inner (1) and outer (2) cylindrical vessel; 3 multiplate supports; 4 and 10 aluminium segments; 5 copper bar; 6 cryostat with LN_2; 7 electrode system; 8 HV connector; 9 xenon supply tube; 11 zeolite trap.

Fig. 2 Schematic view of the electrode connection for spatial-resolution measurements.

Fig. 3 Electrical scheme of the calorimeter.

Fig. 4 Gas system of the calorimeter: 1 test ionization chamber; 2 discharge purifier; 3 calcium reactor; 4 porous-titanium filters; 5 Xe gas storage; 6 LXe calorimeter; 7 zeolite traps; 8 ion pump; 9 vacuum gauge; 10 vacuum pump.

Fig. 5 Schematic view of the beam layout for the investigation of the LXe calorimeter properties. D - delay line; SH - shaping; A - linear amplifier; SHA - shaping amplifier; CS - coincidence unit; F - fanout; C - Cherenkov counters; S - scintillation counters; PC - proportional chambers; M - magnet.

Fig. 6 Secondary particle spectrum in the LXe calorimeter.

Fig. 7 Spectrum of 2.25 GeV/c electrons, measured in the LXe calorimeter.

Fig. 8 Spectrum of 5 GeV/c electrons, measured in the LXe calorimeter.

Fig. 9 E – pc distribution for 2.25 GeV/c electrons.

Fig. 10 E – pc distribution for 4.5 GeV/c electrons.

Fig. 11 The dependence of the energy resolution on the electron energy: × represent the experimental points and • the results of Monte Carlo calculations.

Fig. 12 $X_F - X_S$ distribution for 4.5 GeV/c electrons; X_F was determined by the minimum χ^2 method.

Fig. 13 Energy dependence of the spatial resolution: • centre-of-gravity method, ○ minimum χ^2 method; the curves result from Monte Carlo calculations by the centre-of-gravity method (dashed line) and the minimum χ^2 method (full line).

Fig. 14 The coordinate measurements from the LXe calorimeter versus those from the magnetic spectrometer.

Fig. 15 Dependence of electron to hadron rejection factor on electron efficiency.

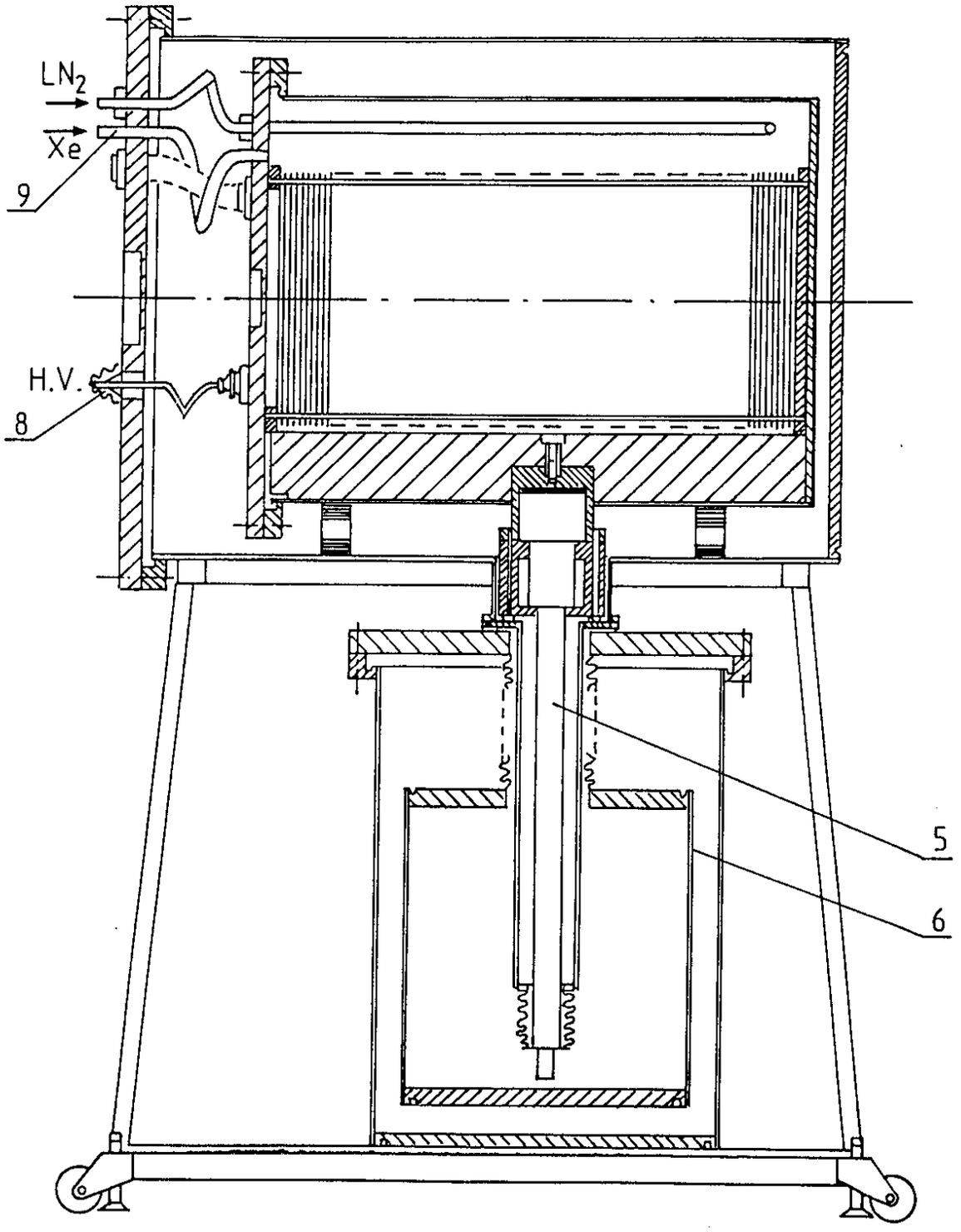

Fig. 1a

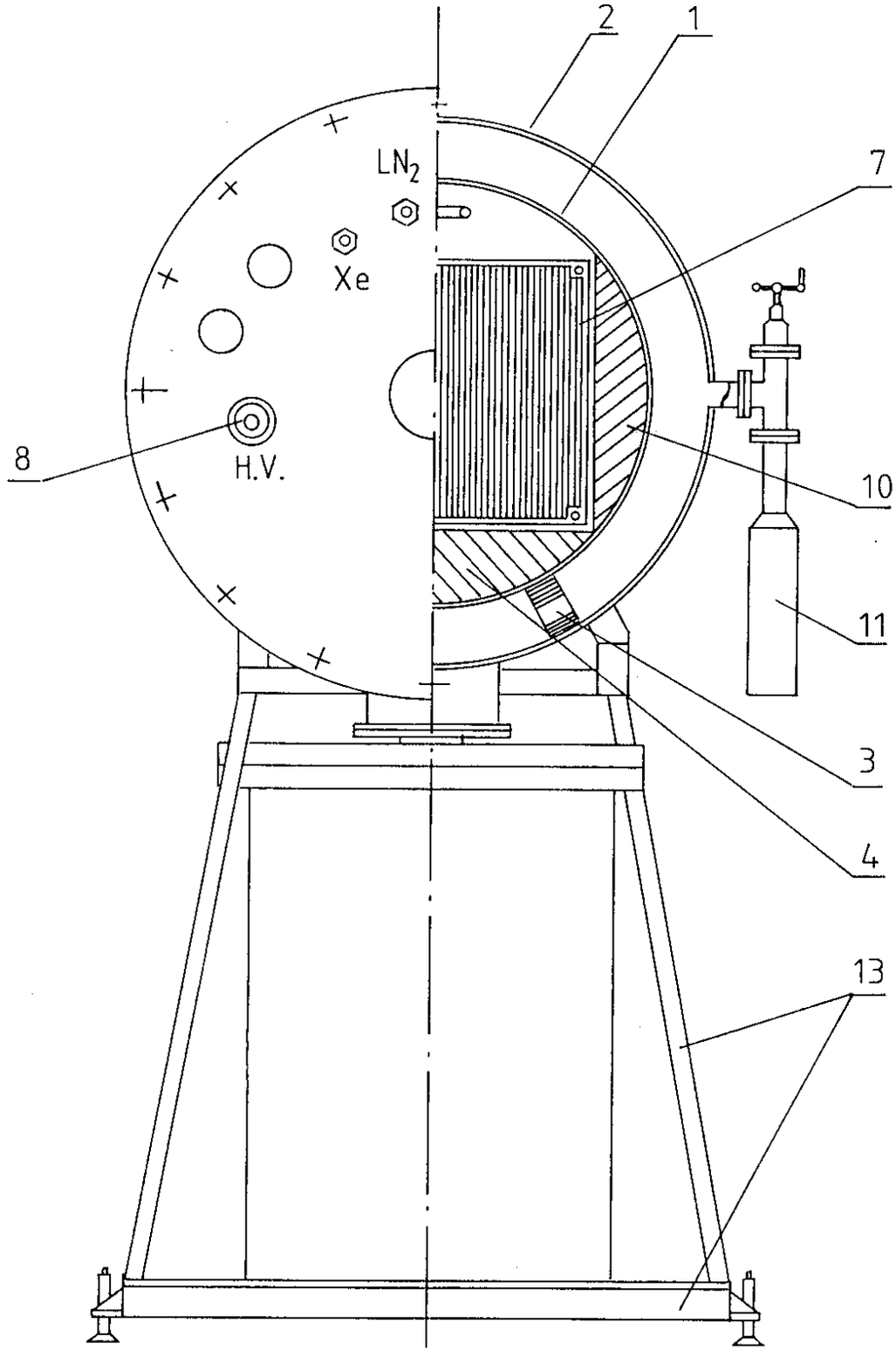

Fig. 1b

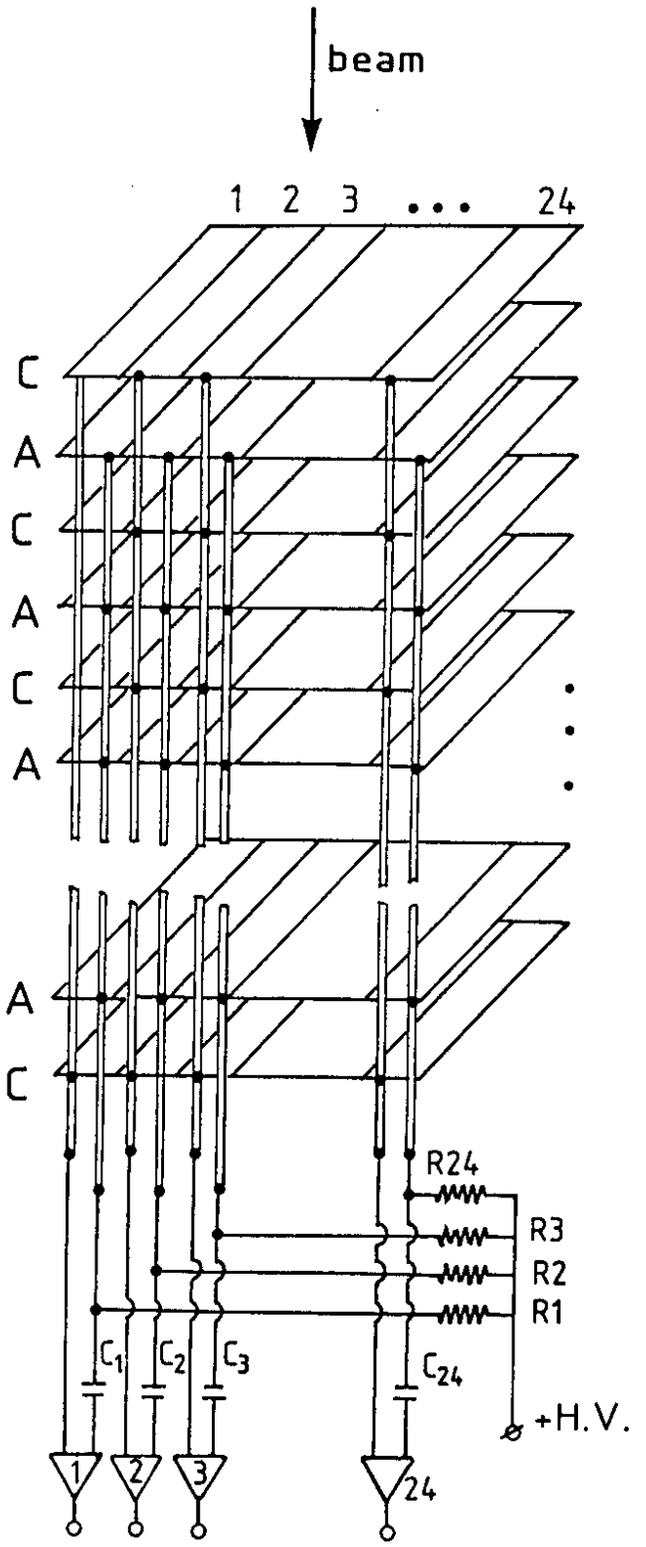

Fig. 2

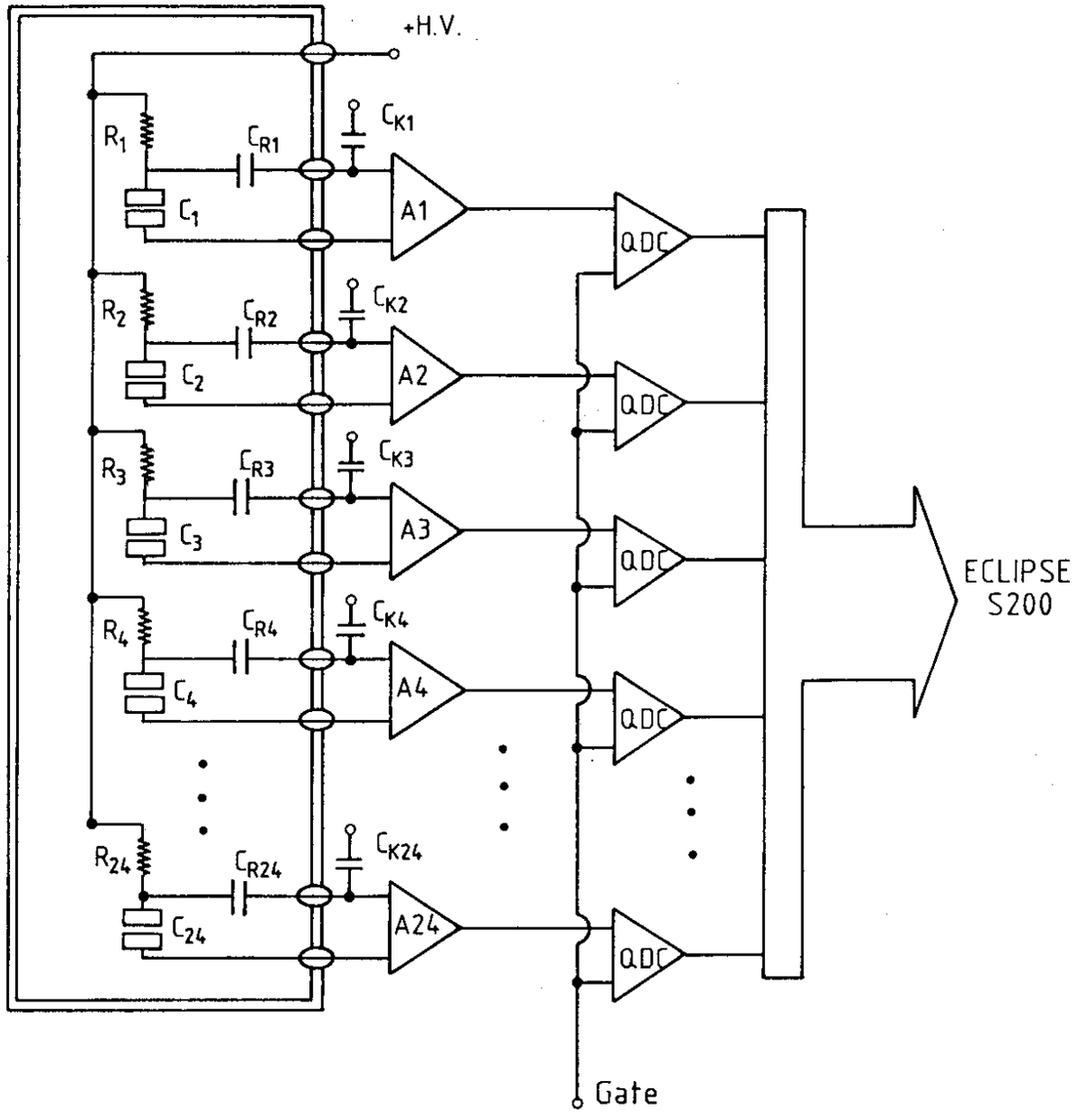
+H.V.
R1
CR1
C1
CK1
A1
R2
CR2
C2
CK2
A2
R3
CR3
C3
CK3
A3
R4
CR4
C4
CK4
A4
R24
CR24
C24
CK24
A24
QDC
QDC
QDC
QDC
QDC
ECLIPSE
S200
Gate

Fig. 3

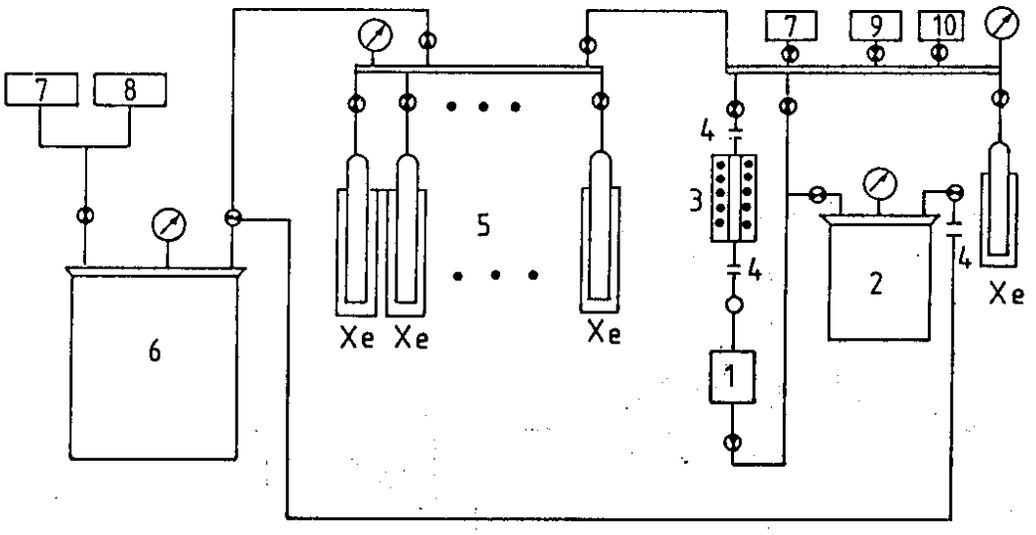
7
8
6
Xe Xe
5
Xe
4
3
4
1
7
9
10
2
4
Xe

Fig. 4

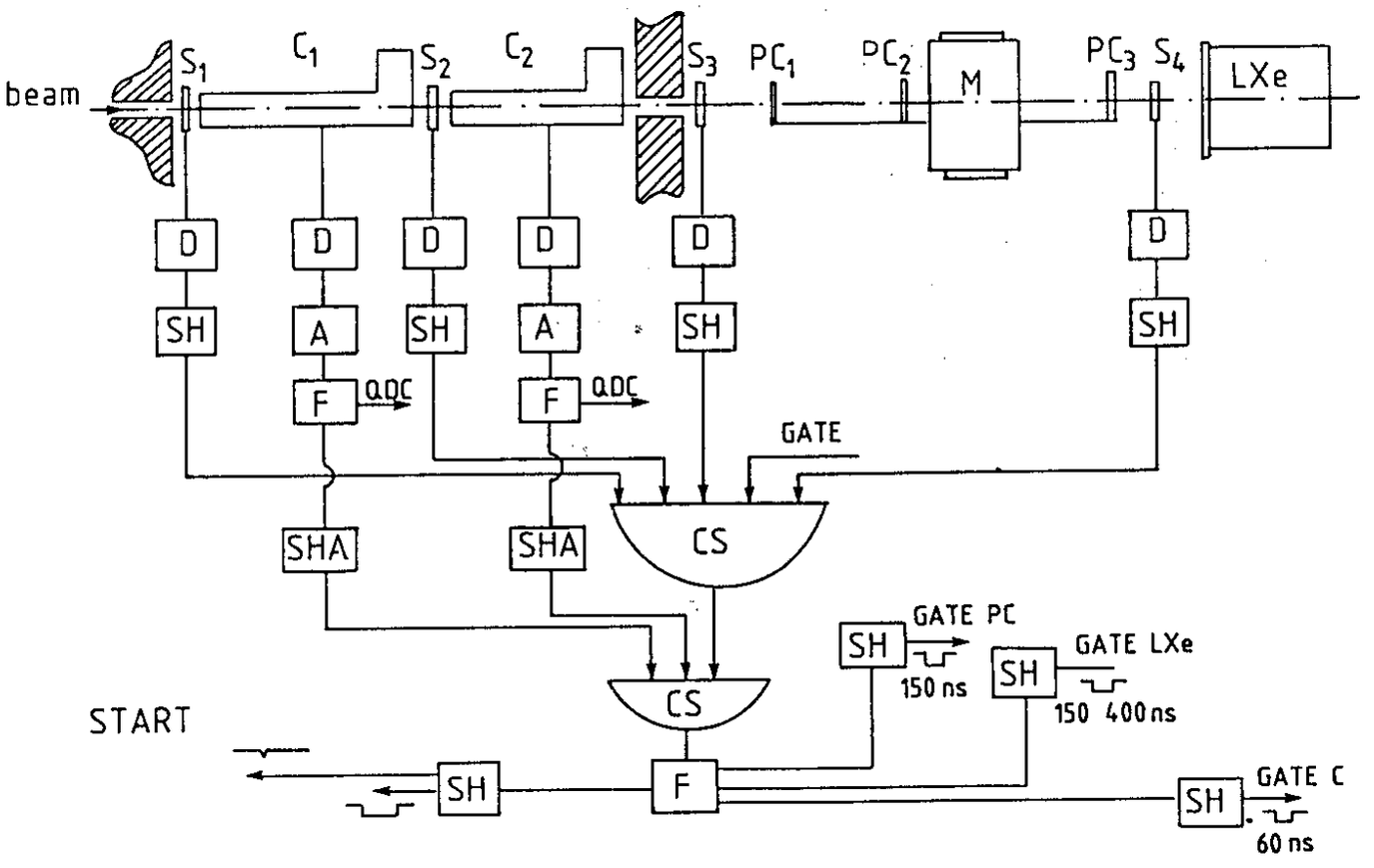
beam
S1
C1
S2
C2
S3
PC1
PC2
M
PC3
S4
LXe
D
SH
A
F
QDC
GATE
SHA
CS
START
GATE PC
150 ns
GATE LXe
150 400 ns
GATE C
60 ns

Fig. 5

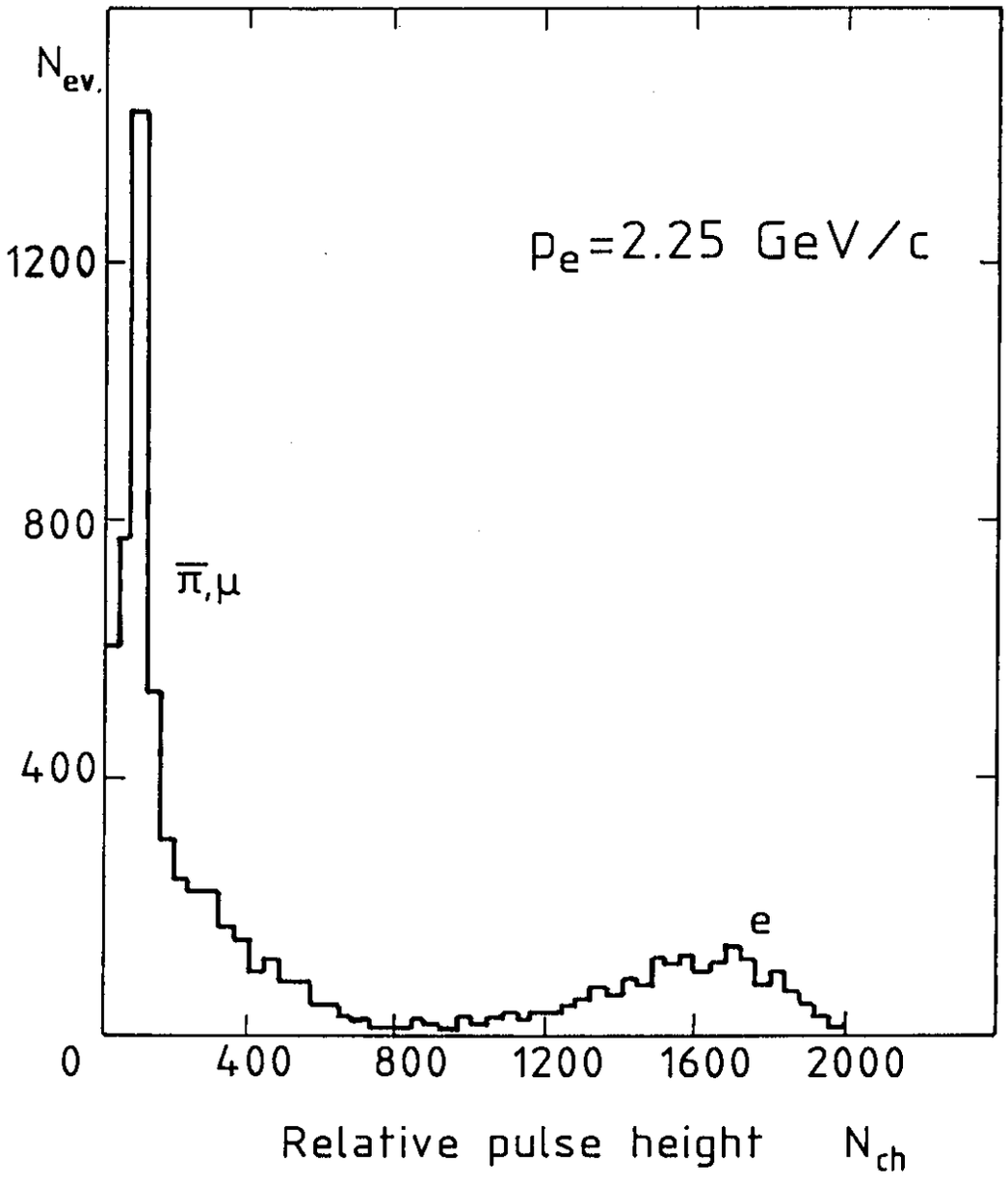
N ev.
1200
800
400
0
400
800
1200
1600
2000
p e = 2.25 GeV/c
π̄,μ
e
Relative pulse height N ch

Fig. 6

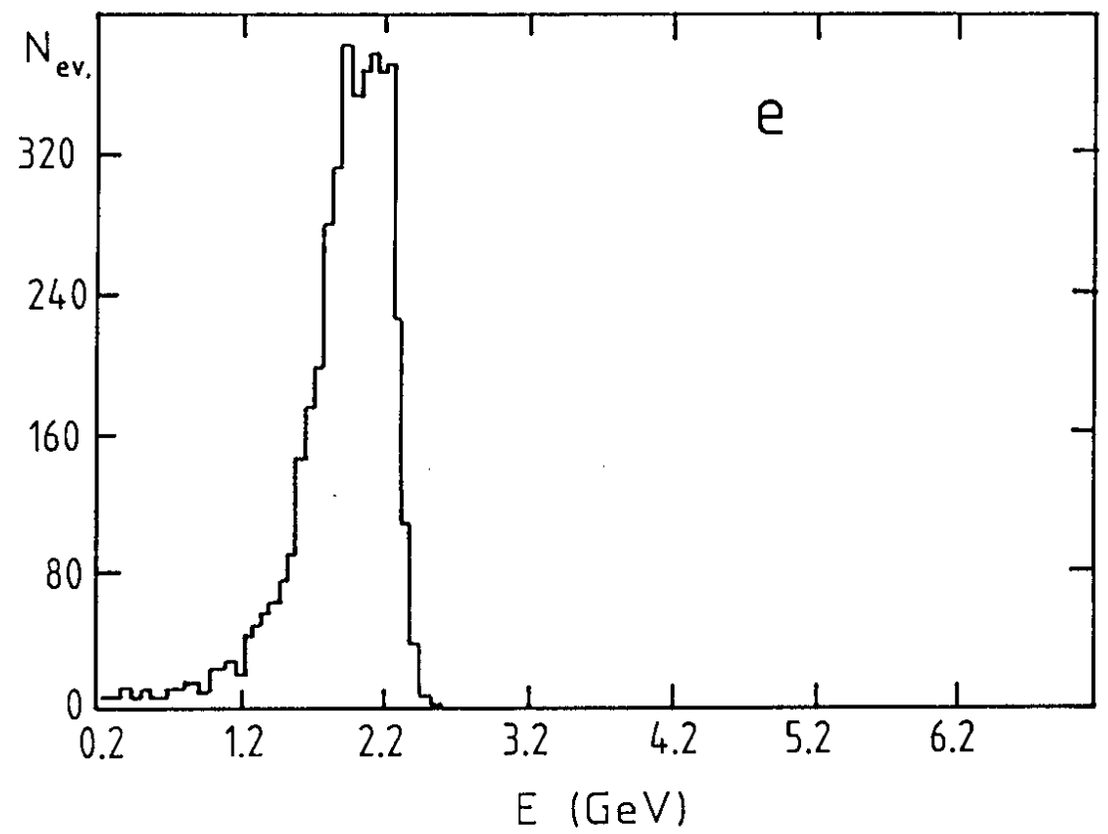
N ev.
320
240
160
80
0
e
0.2
1.2
2.2
3.2
4.2
5.2
6.2
E (GeV)

Fig. 7

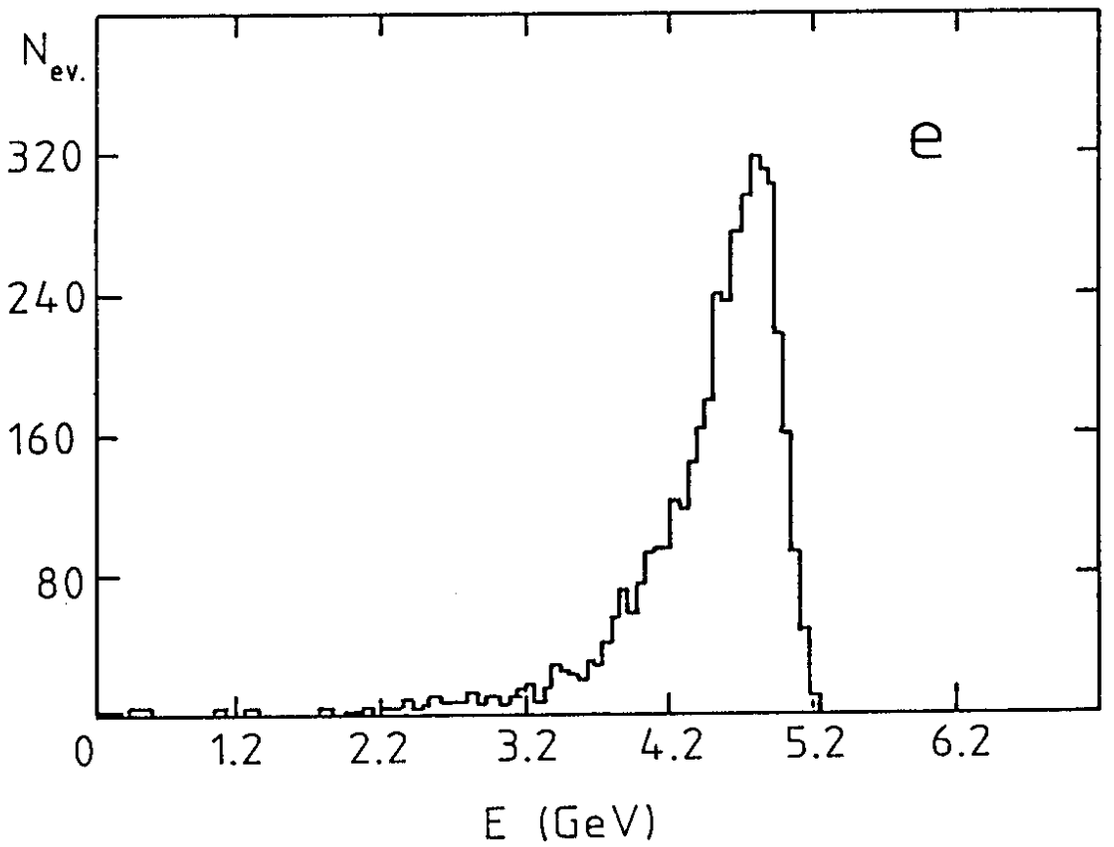
N ev.
320
240
160
80
0
e
1.2
2.2
3.2
4.2
5.2
6.2
E (GeV)

Fig. 8

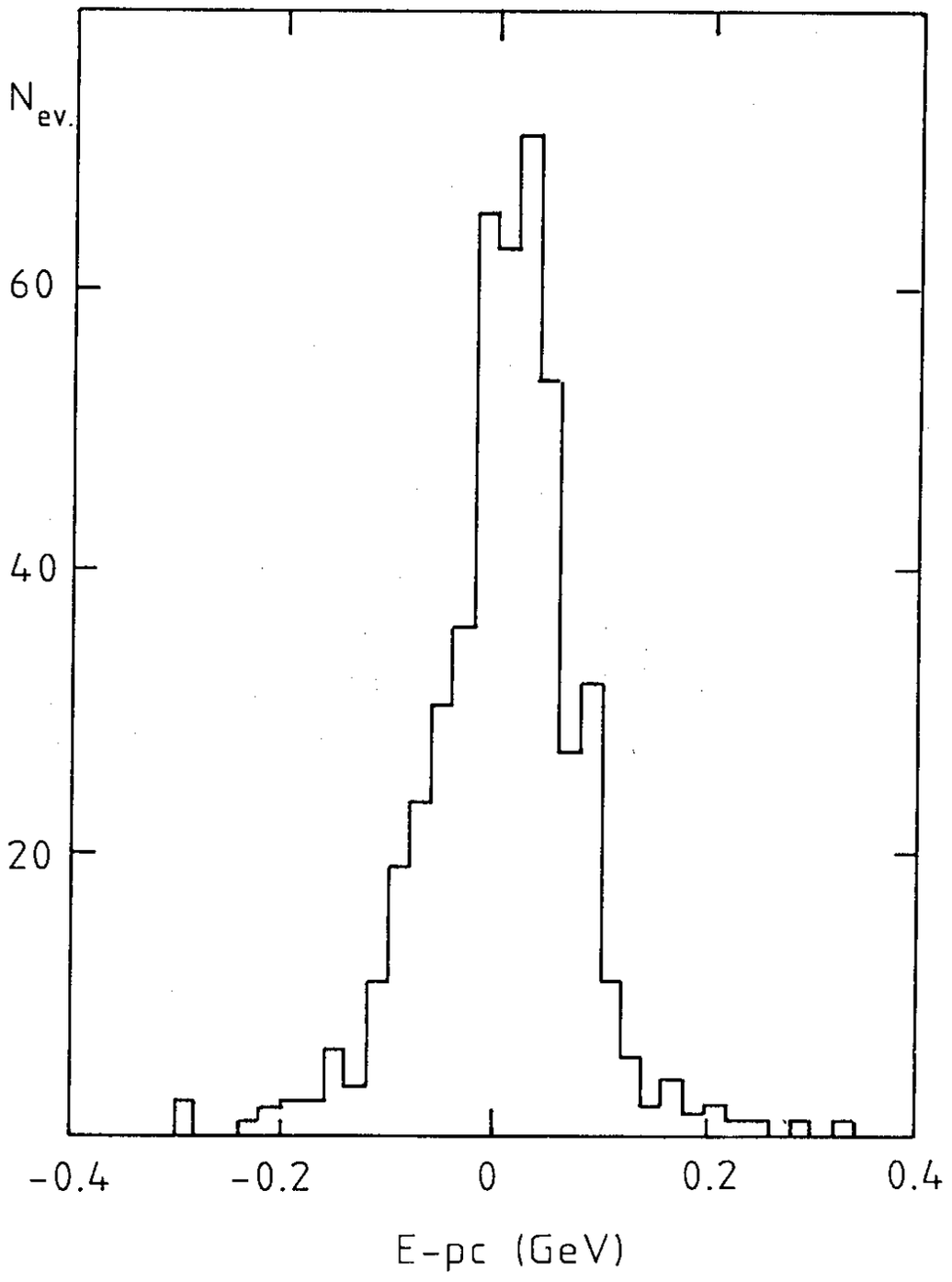

Fig. 9

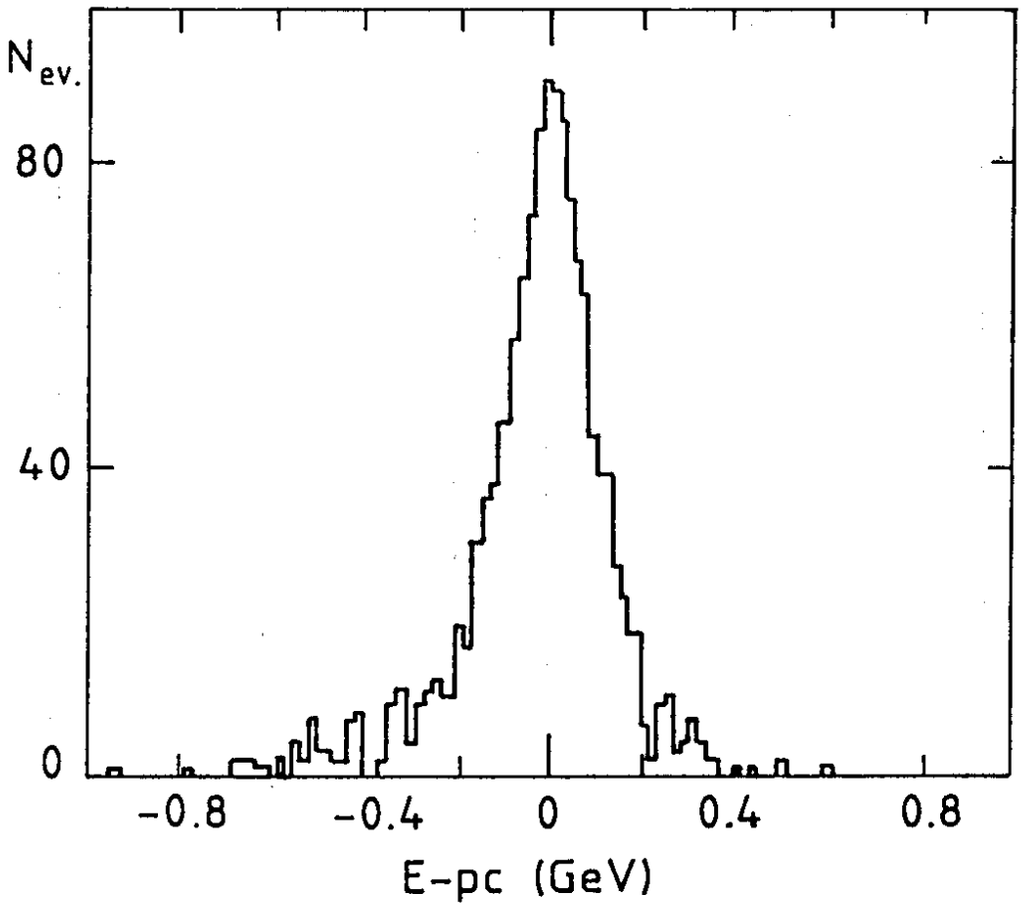

Fig. 10

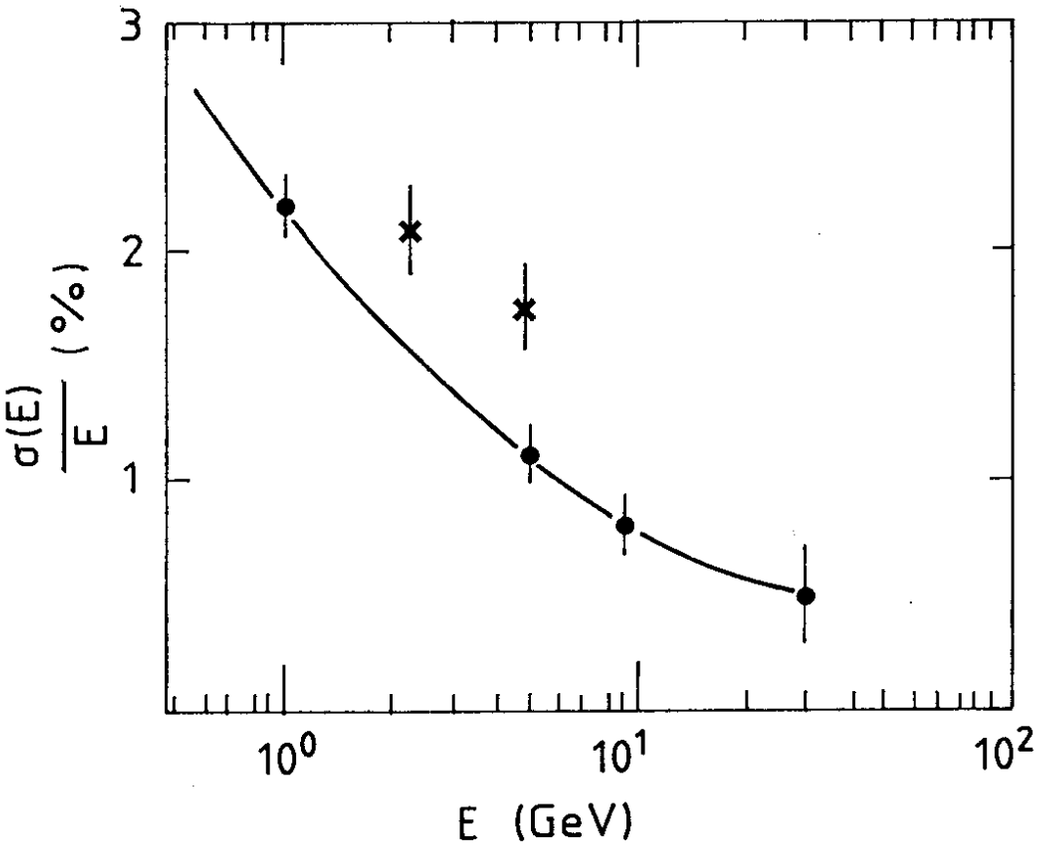

Fig. 11

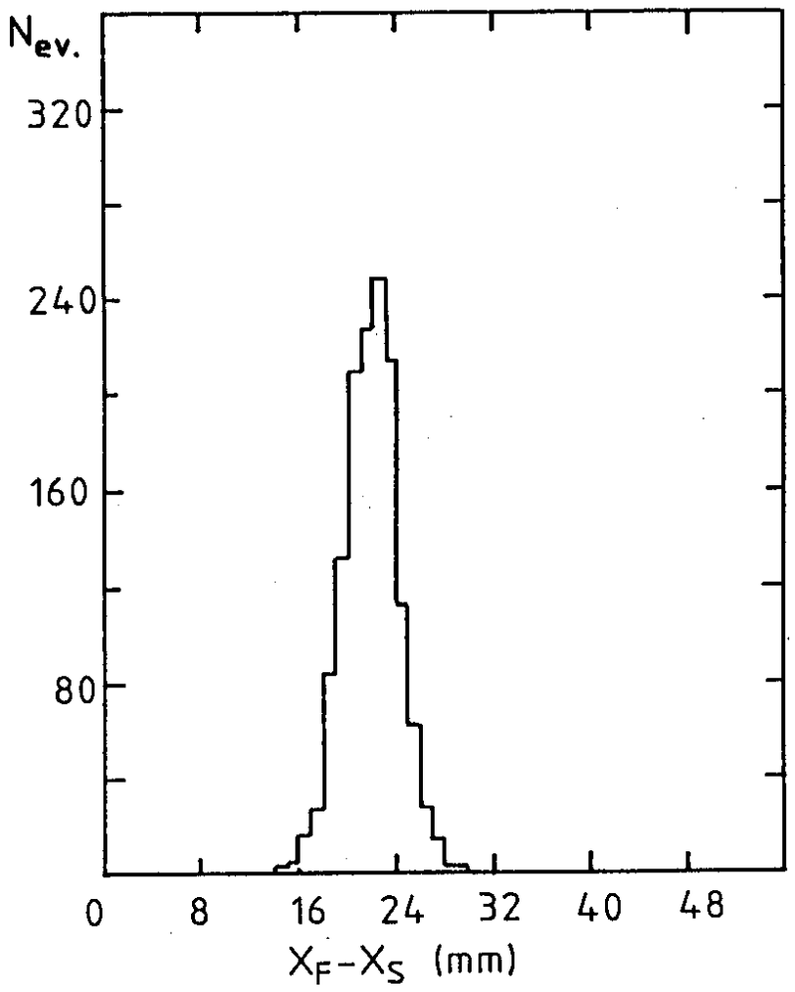

Fig. 12

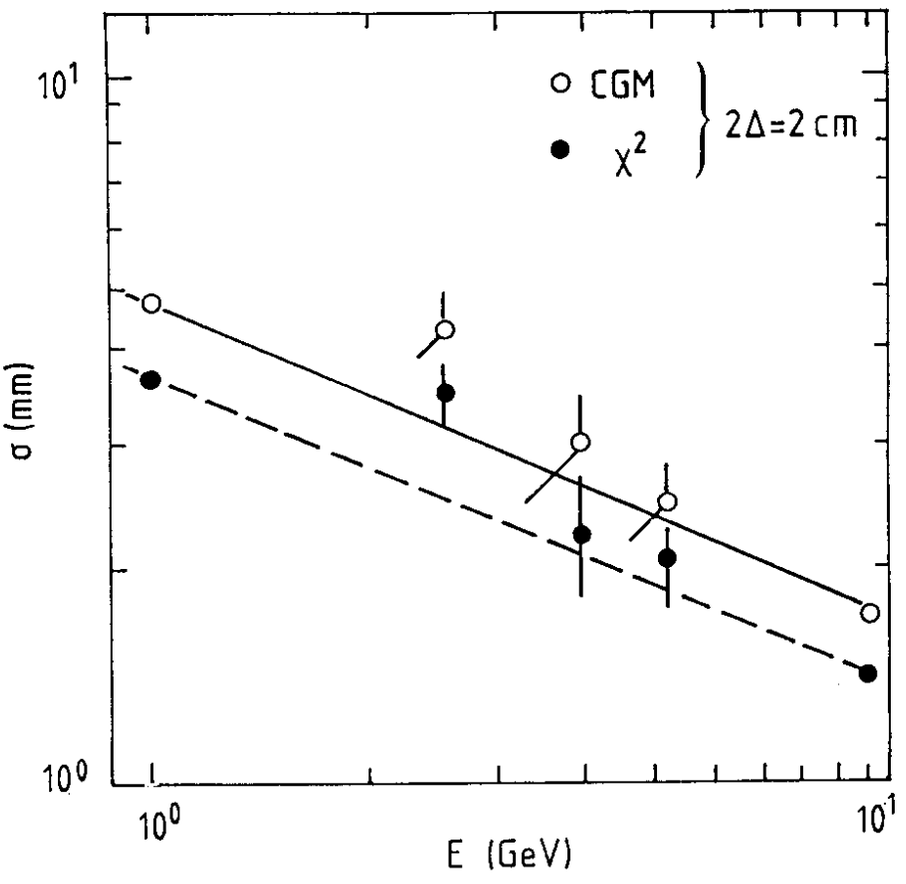

Fig. 13

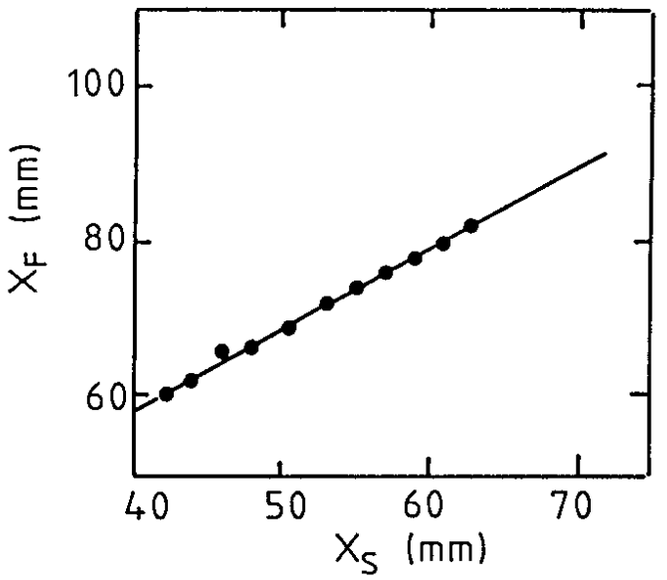

Fig. 14

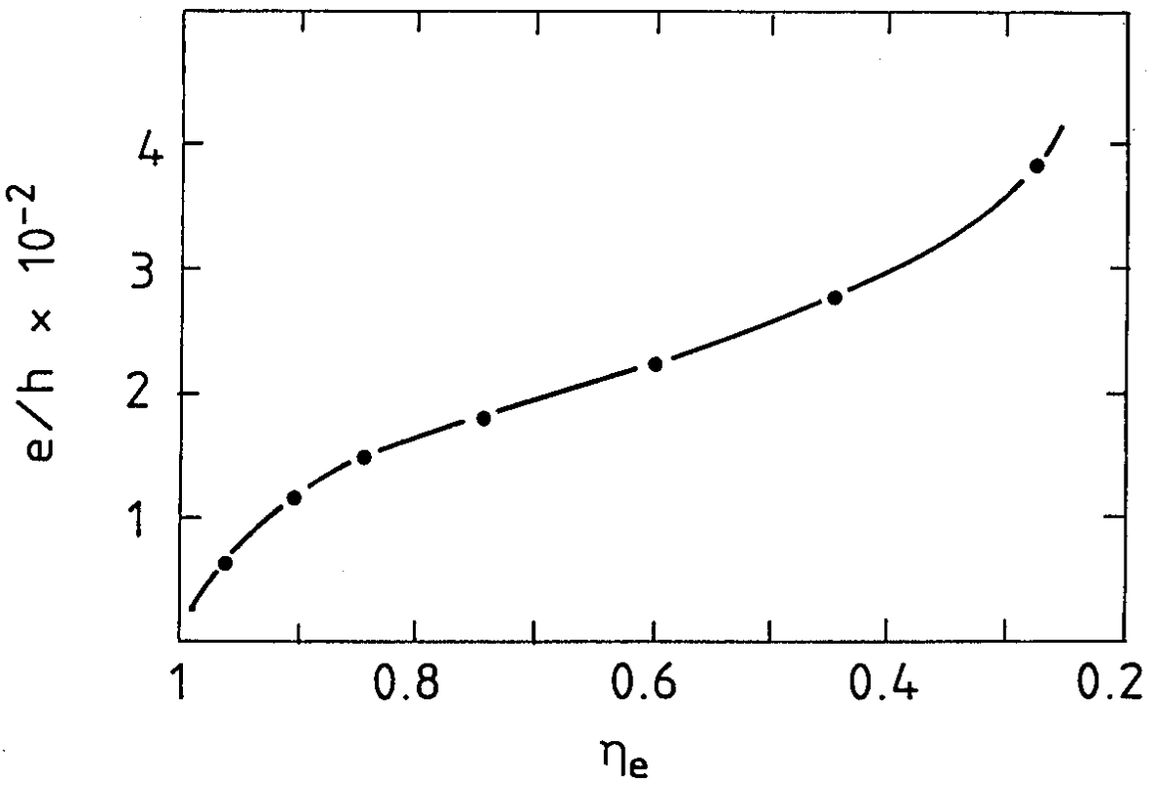

Fig. 15